Available online at www.sciencedirect.com
ScienceDirect
Trans. Nonferrous Met. Soc. China 35(2025) 1197−1211
Transactions of Nonferrous Metals Society of China
www.tnmsc.cn

Influence of processing history on microstructure, mechanical properties, and electrical conductivity of Cu−0.7Mg alloy

Alireza KALHOR[1], Kinga RODAK[1], Marek TKOCZ[1], Bartosz CHMIELA[1], Ivo SCHINDLER[2], Łukasz POLOCZEK[3], Krzysztof RADWAŃSKI[3], Hamed MIRZADEH[4], Marian KAMPIK[5]

1. Faculty of Materials Engineering, Silesian University of Technology, Krasińskiego 8, 40-019, Katowice, Poland;
2. VŠB−Technical University of Ostrava, Faculty of Materials Science and Technology, 17. listopadu 2172/15, 70800 Ostrava, Czech Republic;
3. Materials Research Group, Łukasiewicz Upper Silesian Institute of Technology, Karola Miarki 12-14, 44-100, Gliwice, Poland;
4. School of Metallurgy and Materials Engineering, College of Engineering, University of Tehran, Tehran, Iran;
5. Faculty of Electrical Engineering, Silesian University of Technology, 44-100, Gliwice, Poland

Received 27 September 2023; accepted 4 March 2024

Abstract: The effects of forward extrusion as well as extrusion combined with reversible torsion (KoBo extrusion), followed by additional deformation via the MaxStrain module of the Gleeble thermomechanical simulator, on the microstructure, mechanical properties, and electrical conductivity of a Cu−0.7Mg (wt.%) alloy, were investigated. The simulation results highlighted the critical influence of processing history on determining the equivalent strain distribution. The sample subjected to forward extrusion at 400 °C and subsequent MaxStrain processing (FM sample), possessed 76% lower grain size compared to the sample processed solely with MaxStrain (AM sample). Likewise, the KoBo-extruded and MaxStrain-processed sample (KM sample) exhibited 66% smaller grain size compared to the AM sample. Tensile test results revealed that the AM, FM, and KM samples, respectively, possessed 251%, 288%, and 360% higher yield strength, and 95%, 121%, and 169% higher tensile strength compared to the initial annealed alloy, as a result of grain refinement as well as deformation strengthening. Finally, the electrical conductivity measurements revealed that AM, FM, and KM samples, respectively, possessed electrical conductivity values of 37.9, 35.6, and 32.0 MS/m, which, by considering their mechanical properties, makes them eligible to be categorized as high-strength and high-conductivity copper alloys.

Key words: KoBo extrusion; MaxStrain processing; equivalent strain calculation; grain refinement; tensile properties; electrical conductivity

1 Introduction

Owing to the excellent electrical and thermal conductivities that copper (Cu) and its alloys possess, they are widely used in a variety of industries, including aerospace, electronics, and transportation [1−3]. Although pure Cu has been used for over a century in the electrical sector, new high-tech applications such as electric vehicles and 5G network equipment are increasing the demand for high-strength and high-conductivity (HSHC) Cu alloys that can offer a good combination of improved mechanical properties and high electrical conductivity, simultaneously [4−7]. The term HSHC Cu alloy generally refers to Cu alloys with tensile strengths 1.5−4 times greater than pure Cu (300−800 MPa) and electrical conductivities

Corresponding author: Alireza KALHOR, E-mail: alireza.kalhor@polsl.pl
DOI: https://doi.org/10.1016/S1003-6326(24)66743-9

50%−95% of the international annealed copper standard (IACS) [8].

So far, a wide range of methods have been used for the fabrication of HSHC Cu alloys. Among them, the addition of alloying elements to Cu is a simple but efficient approach for enhancing the mechanical properties of Cu alloys via a combination of different strengthening mechanisms such as solid solution strengthening [9,10], precipitation hardening [11,12], and grain refinement [13,14]. The incorporation of uniformly dispersed nanoparticles into the matrix of Cu alloys is another strategy for enhancing the mechanical performance of these materials [15]. However, improving the mechanical properties of Cu alloys through these methods comes at the cost of decreasing the electrical conductivity [15,16]. Hence, developing reliable techniques as well as improving the current approaches for producing HSHC Cu alloys with minimal or no need for the addition of alloying elements still remains a significant challenge.

In this regard, grain refinement is an effective strategy for improving the mechanical properties of Cu and its alloys without necessarily requiring the addition of alloying elements. It is well known that ultrafine-grained (UFG) materials (with a grain size of 0.1−1 μm) exhibit superior mechanical properties compared to their coarse-grained counterparts [17−19]. Over the last decades, a wide range of grain refinement methods have been developed, including bottom-up approaches like powder metallurgy and top-down strategies such as severe plastic deformation (SPD) techniques [20]. Among these methods, SPD techniques have been proven to be reliable, cost-effective, and promising approaches for fabricating UFG and nanostructured (grain size <100 nm) Cu alloys [21,22].

Prior research has demonstrated the effectiveness of SPD processing in enhancing the mechanical properties of Cu and its alloys. For instance, HIGUERA-COBOS and CABRERA [23] used equal-channel angular pressing (ECAP) for processing electrolytic tough pitch copper, and their ECAP-processed samples exhibited a reduced grain size as well as increased yield strength (YS) and ultimate tensile strength (UTS). In the case of the accumulative roll bonding (ARB) process, it can be referred to the study of LIU et al [24], which found that the hardness and UTS of the oxygen-free high-conductivity copper were increased through the ARB processing. The ARB process also allows for the manufacturing of multi-layered Cu composite structures composed of Cu and other alloys, where the multi-layered structure can exhibit excellent mechanical properties along with high electrical conductivity [25−28].

In another study, ABD EL AAL and KIM [29] fabricated Cu and Cu−SiC composites by powder metallurgy and high-pressure torsion (HPT), and observed that the grain refinement with the formation of bimodal and trimodal microstructures after HPT processing resulted in improved hardness and wear properties of their samples. Likewise, other SPD approaches have also been reported to provide similar benefits in the grain refinement and mechanical properties enhancement of Cu and its alloys. Namely, constrained groove pressing [30], multidirectional forging [31], friction stir processing [32], repetitive corrugation and straightening [33], single-roll angular-rolling [34], twist extrusion [35], and other emerging SPD methods have been successfully used for processing pure Cu as well as a variety of Cu alloys, and the obtained results have shown significant improvements in microstructure and mechanical properties.

Taking into consideration the efficacy of alloying as well as SPD processing, both of these methods were used in the current study to obtain a new HSHC Cu alloy with enhanced properties. For the alloying purpose, Mg was selected because of its relatively lower negative impact on the electrical conductivity compared to other alloying elements such as Ni, Sn, Mn, Al, Co, Fe, and Si [16,36]. Moreover, Cu−Mg alloys constitute one of the primary groups of HSHC Cu alloys that have been successfully used in different industrial sectors, including high-speed railway contact wires [37−40]. Since Mg exhibits a certain level of solubility in Cu [41], when present in small quantities, it only contributes to solid solution strengthening [42]. Therefore, 0.7 wt.% Mg was added to pure Cu to maintain the Cu−Mg alloy within the solid solution range and prevent the formation of the Cu_2Mg intermetallic phase, which reduces the electrical conductivity. Next, forward extrusion as well as extrusion combined with reversible torsion (known as KoBo extrusion), followed by SPD processing using the MaxStrain module of the Gleeble thermomechanical simulator, were applied to the

Cu−0.7Mg alloy to achieve both deformation strengthening and grain refinement. The microstructure, mechanical properties, and electrical conductivity of the fabricated samples were evaluated via a series of experiments, and the obtained results are presented and discussed.

2 Experimental

2.1 Material fabrication

The Cu−Mg alloy was produced by melting rods of pure Cu and Mg (both with a purity of 99.99 wt.%) in a boron nitride-coated graphite crucible inside an induction furnace under a constant flow of Ar gas. The melt was then cast into a preheated steel mold with an internal diameter of 43 mm and a length of 200 mm, and air cooled to room temperature (RT). To achieve alloy homogeneity, the as-cast ingots were annealed at 650 °C for 90 min, followed by air cooling to RT. Then, billets of 100 mm in length were cut from the center of the annealed ingots and machined to the diameter of 39.5 mm to eliminate the casting surface defects as well as provide the required specification for the subsequent extrusion processes. The chemical composition of the alloy is presented in Table 1, and the macrostructure of the as-cast ingot is shown in Fig. 1.

Table 1 Chemical composition of as-cast ingot

Composition	Mass fraction/%	Atomic fraction/%
Cu	99.3±0.1	98.3±0.1
Mg	0.7±0.1	1.7±0.1
Impurities	<0.01	<0.01

2.2 Extrusion processes

By taking into account the fact that the billets first expanded to fill the entire capacity of the container prior to the commencement of the extrusion process, a reduction in the cross-sectional area occurred from the initial circular-shaped cross section with a diameter of 40 mm (~1257 mm^2) to the final square-shaped cross section with a side length of 10 mm (100 mm^2). Therefore, the extrusion ratio (R=A_0/A_e, where A_0 and A_e represent the initial and extruded cross-sectional areas, respectively) for both forward extrusion and KoBo extrusion was ~12.6 based on the configuration used for this study. Thanks to the oscillation of the reversibly rotating die, which reduces the required extrusion force [43], the KoBo extrusion was successfully performed at RT. However, in the case of the forward extrusion, the billet was preheated to 400 °C to facilitate the extrusion process.

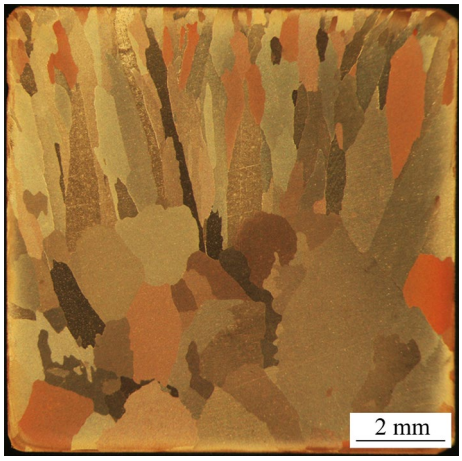

Fig. 1 Macrostructure of as-cast ingot

Figure 2 depicts a simplified schematic illustration of the various components of the KoBo extrusion equipment. This method combines primary deformation from forward extrusion with additional deformation via oscillation of the die at the end of the extrusion container, which results in the material simultaneously undergoing plastic deformation through both regular forward extrusion and reversible plastic twisting via cyclic changes in the deformation path [44−46]. During the KoBo extrusion process, several process variables, such as the punch speed, shape and internal diameter of the container and the reversibly rotating die, oscillation frequency, and oscillation angle, affect the equivalent strain in the extruded component. Any modification in these variables alters the equivalent strain inside the extruded billet, and consequently, affects the microstructure and properties of the final product [47]. In this study, the punch speed was set to be 0.5 mm/s, and the reversibly oscillating die was arranged to rotate at a frequency of 6 Hz with an oscillation angle of ±8°. The billets were pressed

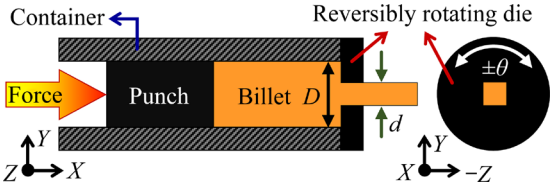

Fig. 2 Simplified schematic illustration of various components of KoBo extrusion equipment

using a hydraulic press with a capacity of 1.5 MN, with molybdenum disulfide (MoS_2) used as a lubricant to reduce friction between the billets and the extrusion container.

2.3 MaxStrain process

For the final stage of deformation, both forward-extruded and KoBo-extruded samples, as well as one sample from the annealed condition, underwent 40 passes of MaxStrain processing at RT. A simplified schematic illustration of the MaxStrain module of the Gleeble thermomechanical simulator is shown in Fig. 3. The MaxStrain process includes controlled deformation of a square cuboid sample by pressing the central region of the sample via two opposing anvils in 180° opposite directions. After the first compression, the sample rotates 90° along its longitudinal axis and is pressed again in the direction perpendicular to the initial compression direction, and this cycle is repeated until the desired amount of accumulated strain is achieved within the sample [48,49]. During the MaxStrain deformation, force, strike, anvil speed, and temperature are the primary process variables that can be precisely controlled [50].

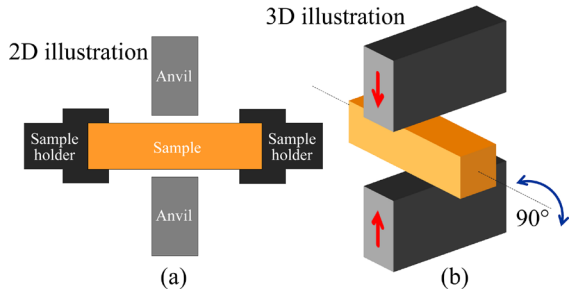

Fig. 3 Simplified schematic illustration of MaxStrain module of Gleeble thermomechanical simulator in 2D (a) and 3D (b) perspectives

The MaxStrain sample can be constrained at its two side ends or left to expand during the deformation (unconstrained or free ends) [51]. When the sample undergoes deformation under the constrained condition, the material flows in transverse directions, whereas in the unconstrained condition, it predominantly flows in longitudinal direction. Consequently, the length of constrained sample remains nearly unchanged after the deformation, while the length of unconstrained sample increases. In this study, the MaxStrain process was performed under an unconstrained condition, with MoS_2 utilized as a lubricant at two side ends of the sample holders to minimize the friction. Table 2 provides a summary of the processing steps along with abbreviated names assigned to each fabricated sample.

Table 2 Summary of processing history and abbreviated names of samples

Processing history	Sample
As-cast alloy → Annealing at 650 °C for 90 min → Air cooling to RT	Annealed alloy
Annealed alloy → MaxStrain processing at RT	AM
Annealed alloy → Forward extrusion at 400 °C → MaxStrain processing at RT	FM
Annealed alloy → KoBo extrusion at RT → MaxStrain processing at RT	KM

2.4 Simulation of deformation processes

The calculation of equivalent strain generated by deformation processes was conducted using the FORGE® NxT simulation software (Version 3.2). For this purpose, first both forward extrusion and KoBo extrusion processes were individually simulated, and the data acquired from these simulations were subsequently employed as input data for simulating the MaxStrain process. To ensure comparability of the results, identical meshing specifications were adopted for simulating the MaxStrain process. Moreover, the simulation variables were set the same as those of the actual deformation processes in order to assure the reliability of the results.

2.5 Material characterization

For microstructural analysis, the samples were cut using an electrical discharge machining apparatus equipped with a 0.3 mm brass wire, and prepared using the conventional approach of abrasion and polishing, followed by etching in an etchant consisting of 5 g $FeCl_3$ + 3 mL HCl + 97 mL ethanol for 5−10 s. A Hitachi S−3400N scanning electron microscope (SEM) with a primary electron beam energy of 15 keV was used for both the EDS analysis and the fractography. The electron backscatter diffraction (EBSD) maps were taken with an Inspect JEOM JSM−7100F SEM equipped with an EDAX camera at 20 kV accelerating voltage, and the EBSD data were processed with the OIM TSL software. To ensure the accuracy of the EBSD results, a post-processing

step that included a single iteration of grain dilation clean-up and confidence index standardization was performed as well.

2.6 Assessment of mechanical properties

The mechanical properties of the samples were assessed through hardness and tensile tests. The hardness test was performed using the Vickers method with a load of 1 kg (HV_1) and a dwelling duration of 10 s using the Struers Duramin A300 hardness tester. Due to the limited dimension of the deformation zone in MaxStrain-processed samples, tensile tests were carried out on minisamples, as shown in Fig. 4(a). These minisamples were cut precisely from the central regions of deformation zones and oriented perpendicular to the 40th pass pressing direction, as illustrated in Fig. 4(b). The tensile tests were performed at RT using an MST QTest/10 device with an initial strain rate of 1×10^{-3} s^{-1} and three repetitions for each sample.

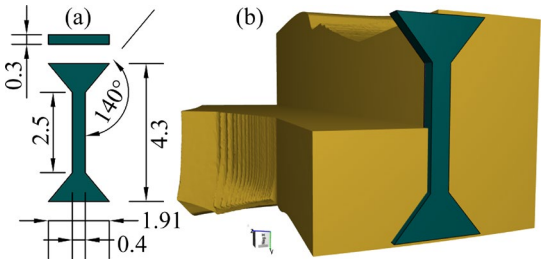

Fig. 4 Dimensions (a) and position (b) of minisamples used for performing tensile test (Unit: mm)

2.7 Evaluation of electrical conductivity

The electrical conductivity of the samples was assessed using the 4-wire Kelvin resistance measurement method, with samples having a cross-sectional area of ~2 mm^2 and a length of 4 mm cut in the same direction as the tensile test minisamples. This approach involves using four evenly placed probes (two for current injection and two for voltage sensing) to apply a specified current and measure the resultant voltage, allowing the electrical resistivity of the material to be calculated [52]. For the current source, the Fluke 5700A calibrator was used, and for measuring the voltage along the samples, the Keithley 2182A nanovoltmeter was employed. During the test, it was observed that currents exceeding 1 A led to a minor temperature rise, and currents below 200 mA caused a comparable influence of thermal electro-motive force. Consequently, the test current was adjusted to 750 mA for most effective evaluation conditions, and each sample underwent four measurements at RT. Figure 5 depicts a simplified schematic illustration of the 4-wire Kelvin resistance measuring setup.

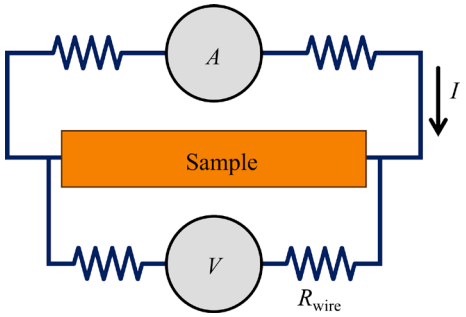

Fig. 5 Simplified schematic illustration of 4-wire Kelvin resistance measurement setup

According to Ohm's law, the resistance (R, Ω) of a conductor is equal to the voltage (V, V) across the conductor divided by the current (I, A) flowing through it, as presented in Eq. (1):

$$R=V/I \tag{1}$$

The resistivity (ρ, Ω·m) and R are related by

$$\rho=RA/L \tag{2}$$

where A represents the cross-sectional area of the conductor (m^2) and L represents its length (m).

The electrical conductivity (σ, S/m) is defined as the inverse of the ρ as follows:

$$\sigma=1/\rho \tag{3}$$

3 Results and discussion

3.1 Calculation of equivalent strain

3.1.1 Extrusion processes

The simulation results for both forward extrusion and KoBo extrusion processes are displayed in Fig. 6. As shown in Figs. 6(a, b), the distribution of equivalent strain in the initial product of extruded billets was not homogeneous for both extrusion processes. Consequently, these initial segments of the extruded billets were excluded from subsequent analysis. Moreover, despite using the same extrusion ratio for both the forward and KoBo extrusion processes, different values of equivalent strain were attained within the extruded billets. Figures 6(c, d) show that the

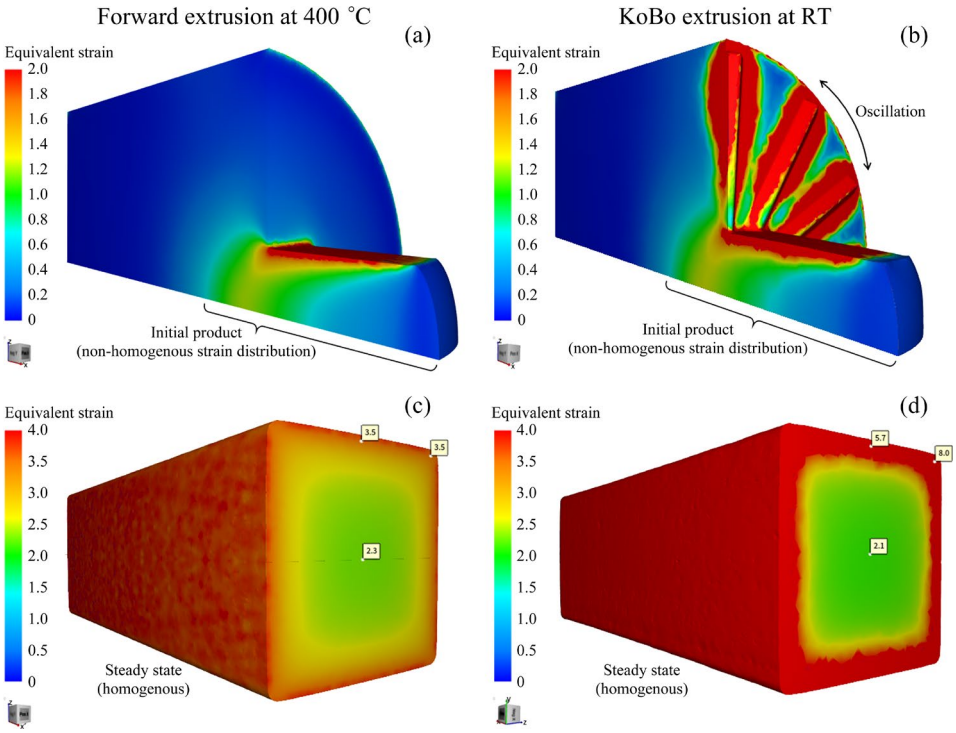

Fig. 6 Distribution of equivalent strain in initial product of forward extrusion (a) and KoBo extrusion (b), and in steady state part of forward-extruded (c) and KoBo-extruded (d) billets

maximum equivalent strain was attained at the edges and corners of the forward-extruded billet, and the corners of the KoBo-extruded billet. It can be seen that the calculated value was higher at the edges and corners of the KoBo-extruded billet compared to the forward-extruded billet, which is indeed the consequence of the plastic twisting induced by the oscillation of the reversibly rotating die in the KoBo extrusion process.

In addition, the equivalent strain was computed to be 2.3 in the center of the forward-extruded billet, which is ~10% higher than the calculated equivalent strain of 2.1 in the center of the KoBo-extruded billet, which can be ascribed to the deformation temperature. In fact, the relatively high deformation temperature in the forward extrusion process led to a greater material flow in this process, which caused a higher equivalent strain in the center of the forward-extruded billet. The results for the steady state part of the extruded billets (Figs. 6(c, d)) were cut out and used as input data for the simulation of the MaxStrain process.

3.1.2 MaxStrain processing

In order to obtain more reliable results from the simulation of the MaxStrain process, the values of the ultimate height of the anvils for each pass were acquired from the experimental data and used to determine the anvil displacement per pass. In other words, the simulation was carried out using a constant starting height for the anvils, set at 8 mm above the surface of the undeformed sample (equivalent to the distance of 13 mm from the center of the sample), and their ultimate height at the end of each pass. The strike pattern versus the operation time used in this study to perform the MaxStrain process is displayed in Fig. 7. With the simulation results from the extrusion processes as input data for modeling the MaxStrain process, the cumulative equivalent strain inside the samples after MaxStrain processing was calculated.

Figures 8(a, b, c) show the simulation results for 1/2 of the AM, FM, and KM samples, with the central transverse cutting plane applied to the center of their deformation zones to allow for the observation of the distribution of equivalent strain within the center of the samples. The results show that the initial variations in the distribution of equivalent strain within the extruded billets led to a distinctly different gradient of equivalent strain following the MaxStrain processing. The AM sample achieved a maximum equivalent strain of 5.0 at the center and a minimum equivalent strain of

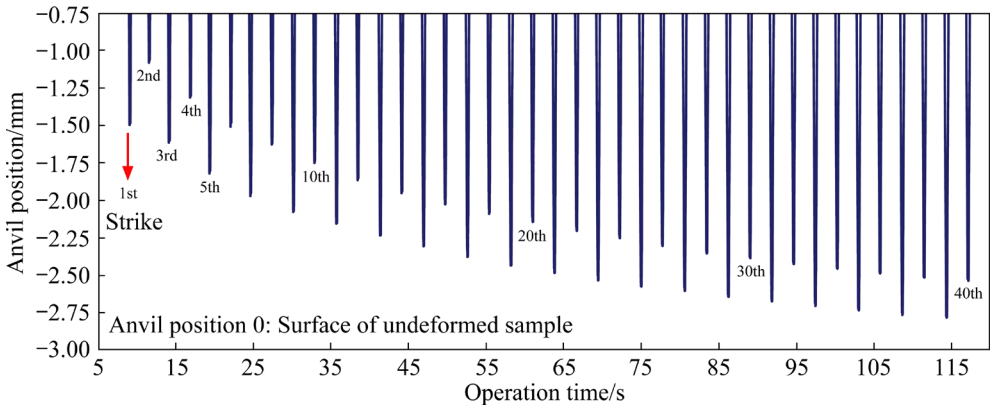

Fig. 7 Strike pattern used for performing MaxStrain process

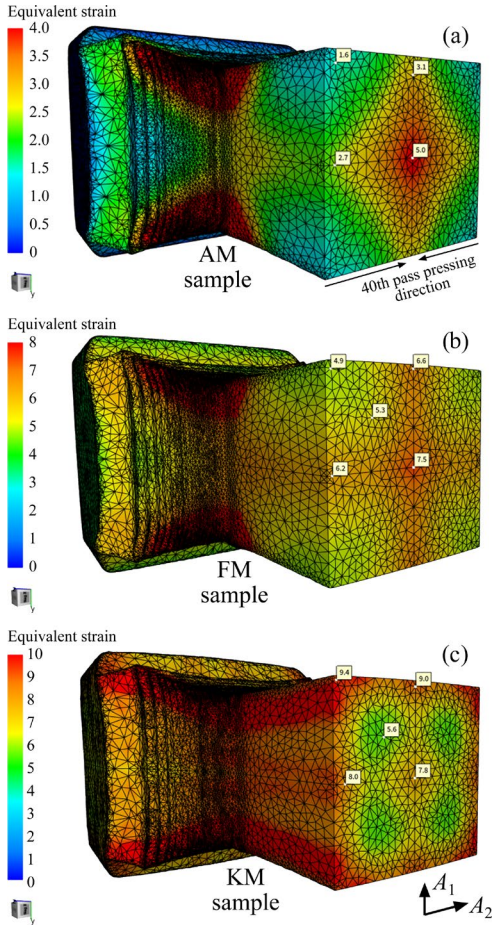

Fig. 8 Distribution of equivalent strain in AM (a), FM (b), and KM (c) samples

1.6 at a location near the corner of the central transverse plane (Fig. 8(a)). It is notable to mention that due to the characteristics of MaxStrain processing, which involves the application of plastic deformation in two perpendicular directions, it resulted in different calculated equivalent strains at the adjacent edges.

The equivalent strain distribution within the central transverse plane of FM sample resembled that of the AM sample, featuring a peak calculated equivalent strain of 7.5 at the center, a minimum of 4.9 at the corner, and calculated values of 6.6 and 6.2 at the edges of the same plane (Fig. 8(b)). In the meantime, the KM sample exhibited a different distribution of equivalent strain. The maximum equivalent strain value at the corner and the edge of the initial KoBo-extruded billet further increased after MaxStrain processing, which resulted in the maximum equivalent strain of 9.4 at the corner of the central transverse plane and the minimum equivalent strain of 5.6 at a location approximately half the distance between the center and the corner (Fig. 8(c)). These results underscore the paramount importance of processing history in determining the finally achieved equivalent strain, in which the dissimilar distributions of equivalent strain in forward-extruded (Fig. 6(c)) and KoBo-extruded (Fig. 6(d)) samples led to entirely different equivalent strain distributions following MaxStrain processing in FM (Fig. 8(b)) and KM (Fig. 8(c)) samples.

3.2 Microstructures following deformation

The inverse pole figure (IPF) maps captured from the center of the central transverse plane at the deformation zone of the MaxStrain-processed samples are shown in Figs. 9(a−c). The lengths of the images are perpendicular to the direction of the 40th pressing pass, and high-angle grain boundaries (HAGBs, $\theta \geq 15°$) are indicated by black lines. Using EBSD quantitative data, the average grain size was measured to be 5.8 μm for the AM sample, 1.4 μm for the FM sample, and 2.0 μm for the KM sample at the center of the central transverse plane. During

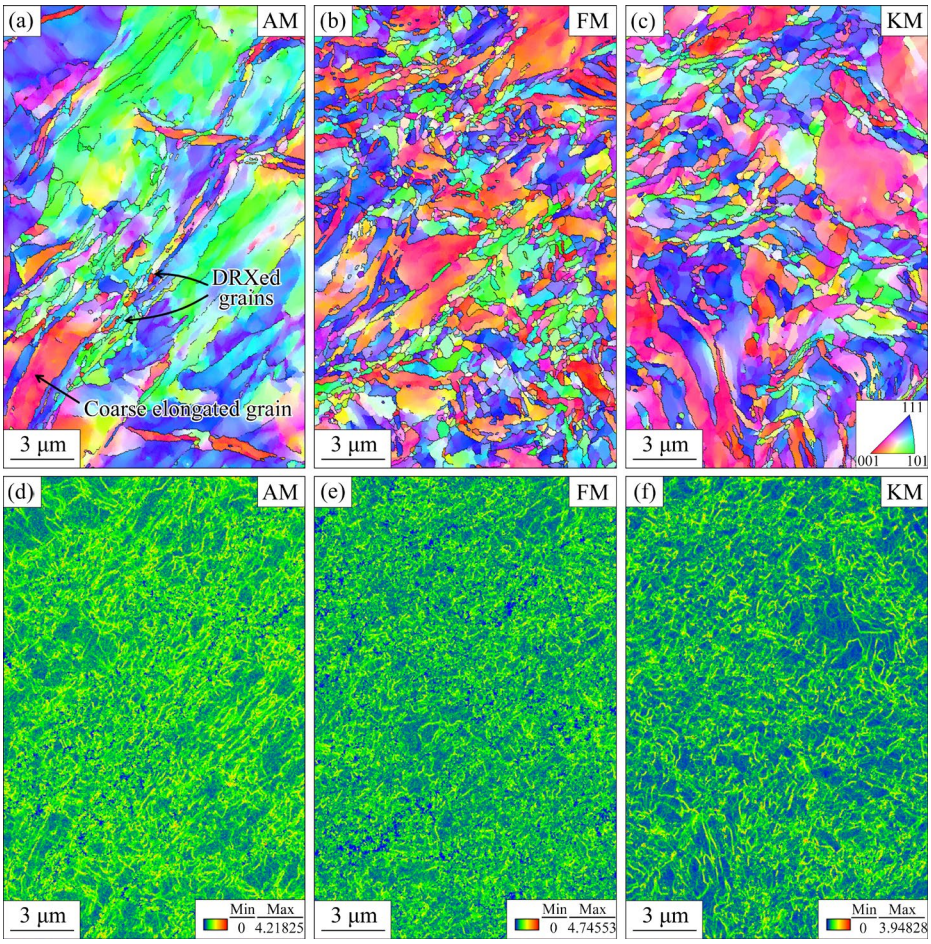

Fig. 9 IPF maps of AM (a), FM (b), and KM (c) samples, and KAM maps of AM (d), FM (e), and KM (f) samples

deformation in both extrusion processes as well as MaxStrain processing, the primary mechanism responsible for grain refinement was dynamic recrystallization (DRX). In the case of the AM sample (Fig. 9(a)), the heterogeneous grain structure consisting of both coarse elongated and fine equiaxed grains indicates the occurrence of partial DRX. This partial DRX is the consequence of performing the MaxStrain process at RT, which is lower than the typical temperature required for the occurrence of DRX in Cu alloys.

In the case of the FM sample, since the forward extrusion was performed at 400 °C (which equals ~0.5T_m of the alloy) prior to MaxStrain processing, this resulted in the occurrence of a relatively higher extent of DRX after the MaxStrain processing. This effect is clearly visible through the higher fraction of fine equiaxed grains in the FM sample (Fig. 9(b)) compared to the AM sample, as well as the 76% lower grain size of the FM sample compared to the AM sample. Interestingly, even though the calculated equivalent strain in the center of the central transverse plane of the KM sample was 4% higher than that of the FM sample, the EBSD results revealed that the KM sample possessed 43% larger grains compared to the FM sample (Fig. 9(c)). This larger grain size in the KM sample despite its higher equivalent strain compared to the FM sample, emphasizes the determinative effect of deformation temperature on the extent of DRX and grain refinement process. Meanwhile, compared to the AM sample, the KM sample exhibited a 66% lower grain size. The kernel average misorientation (KAM) maps for the AM, FM, and KM samples are displayed in Figs. 9(d−f), respectively. Notably, the AM sample, which was characterized by a lower fraction of DRXed grains, exhibited a higher proportion of LAGBs compared to the FM and KM samples, which exhibited a higher fraction of DRXed grains.

Figure 10 presents the distribution of misorientation angles in the AM, FM, and KM samples. A comparison of the misorientation angle distributions reveals a higher fraction of HAGBs

present in the FM and KM samples compared to the AM sample, which is the consequence of the smaller grain size in these samples. This is consistent with the IPF maps showing that the extent of DRXed grains was lower in the AM sample compared to the FM and KM samples.

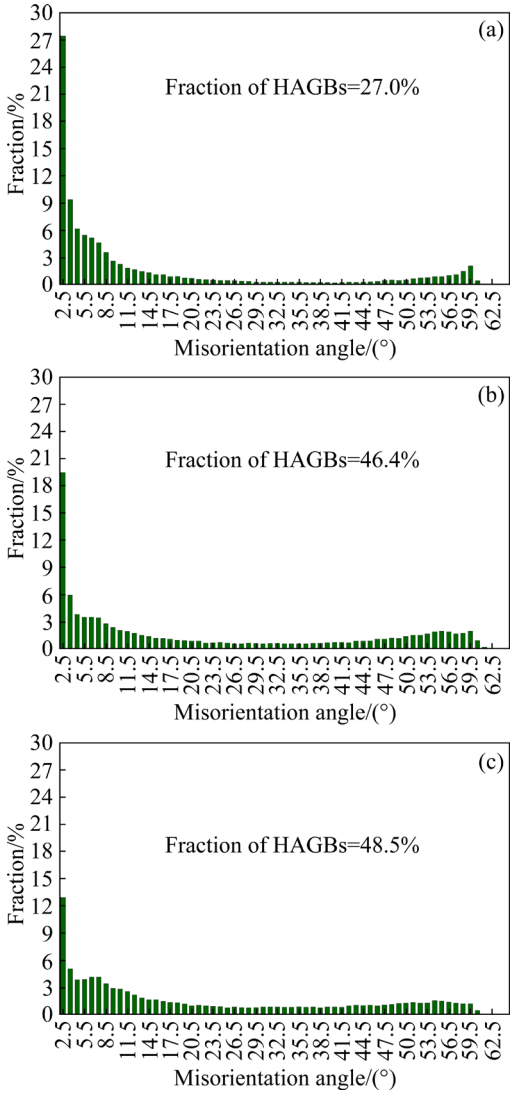

Fig. 10 Distribution of misorientation angles: (a) AM sample; (b) FM sample; (c) KM sample

3.3 Mechanical properties

The hardness test results revealed that the annealed alloy possessed an average hardness value of (59±2) HV. For MaxStrain-processed samples, since it was impractical to announce a single representative value for average hardness due to the strain inhomogeneity within the samples, the indentations were performed along the primary A_1 and A_2 directions shown in Fig. 8(c) within the central transverse plane of the samples. These indentations were carried out at regular intervals of 0.45 mm, and the corresponding hardness values are displayed in Fig. 11. Remarkably, distribution of hardness values within MaxStrain-processed samples matched the equivalent strain distribution pattern obtained from the simulation.

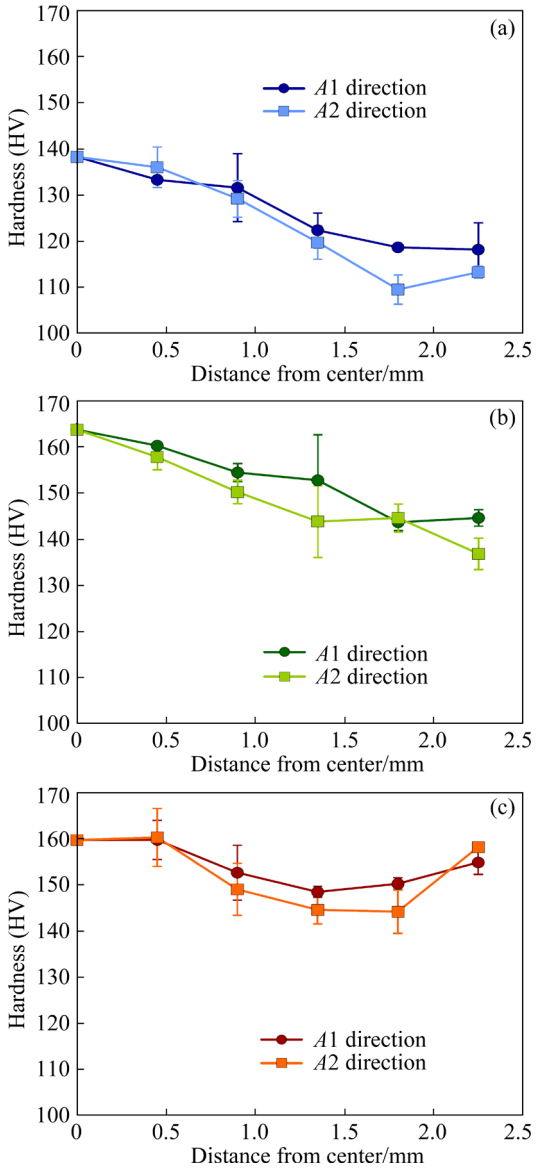

Fig. 11 Hardness profiles for AM (a), FM (b), and KM (c) samples

In the case of the AM sample, a higher hardness value was determined at the central spot (138.3 HV) compared to the middle and edge regions. This difference in hardness comes from the higher equivalent strain at the center, which led to a more pronounced strain hardening effect in that region. The FM sample also exhibited a higher hardness in the center of its central transverse plane (163.7 HV), and the measured hardness values were

constantly lowered by going further from the center towards the edge. Regarding the KM sample, although the highest hardness was recorded at its center (159.7 HV), the edge region of the central transverse plane exhibited a higher hardness compared to the areas between the center and the edge of the sample. Notably, the KM sample displayed better hardness uniformity compared to the FM and AM samples. MOU et al [53] observed a similar correlation between equivalent strain and hardness. In their study, simulation results indicated that the surface region of an H62 brass, subjected to multi-cycle constrained groove pressing, exhibited a higher equivalent strain than its interior, which provided a higher surface hardness.

The tensile test results for the samples are presented in Fig. 12. Due to the limited dimensions of the minisamples used for performing the tensile test, using an extensometer to measure displacement during the tensile test was not possible. Hence, to calculate the percentage of total elongation (EL) for each sample, the lengths of the broken fragments of tensile test samples (shown in Fig. 13) were measured individually and used for the calculation of EL to ensure the reliability of the obtained results. The annealed alloy exhibited a YS of (119±11) MPa, a UTS of (232±15) MPa, and an EL of (33.8±1.6)%, which are typical values for non-deformed Cu−Mg alloys [54,55].

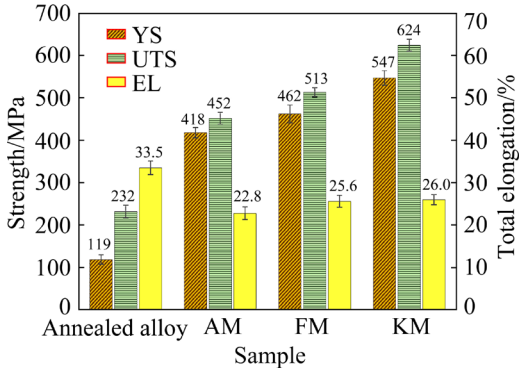

Fig. 12 Data obtained from tensile test results

The tensile test results for the AM sample indicated that MaxStrain processing led to a substantial increase in both the YS and UTS of the annealed alloy, showing improvements of 251% and 95%, respectively. The YS enhancement is primarily attributed to the achievement of a finer grain size through partial DRX induced by MaxStrain processing, based on the principles outlined in the Hall−Petch relationship [56]. Likewise, the enhancement in UTS can be attributed to a combination of factors, including grain refinement, strain hardening, and an increased dislocation density within the sample. Nevertheless, the EL of the AM sample was 32% lower than that of the annealed alloy. The decrease in elongation can be attributed to the increase in crystal defects [57]. This is consistent with the observation that the AM sample, which had the lowest extent of DRXed grains, exhibited the lowest elongation. In contrast, the FM and KM samples with a higher fraction of DRXed grains (which have lower crystal defects) showed slightly higher elongation values.

The tensile test results also revealed that extruding the annealed alloy before MaxStrain processing, either forward extrusion or KoBo extrusion, resulted in further enhancing the mechanical properties of the alloy. The FM sample demonstrated 288% higher YS and 121% higher UTS than the annealed alloy, and the KM sample exhibited 360% higher YS and 169% higher UTS than the annealed alloy. In fact, the application of an extrusion process prior to the MaxStrain deformation led to a higher extent of DRX and a resultant smaller grain size (Fig. 9), as well as a more pronounced strain hardening effect, which contributed to the higher YS and UTS in the FM and KM samples.

The broken pieces and the corresponding fracture surface of the AM sample are respectively displayed in Figs. 13(a) and 13(d), which show a ductile fracture surface containing dimples. Likewise, the fracture surfaces of the FM and KM samples, as shown in Figs. 13(e) and 13(f), respectively, exhibit ductile fractures characterized by dimples. Notably, all samples exhibited a fracture surface characterized by a heterogeneous dimple structure, with big dimples corresponding to coarse-grained areas and small dimples belonging to fine-grained zones. In alignment with the EBSD results shown in Fig. 9, the FM and KM samples, which possessed a higher fraction of fine DRXed grains, showed a higher proportion of fine-sized dimples on their fracture surfaces.

3.4 Electrical conductivity

The measured electrical conductivity values for the samples are presented in Fig. 14. The results show that the conductivity for the annealed alloy

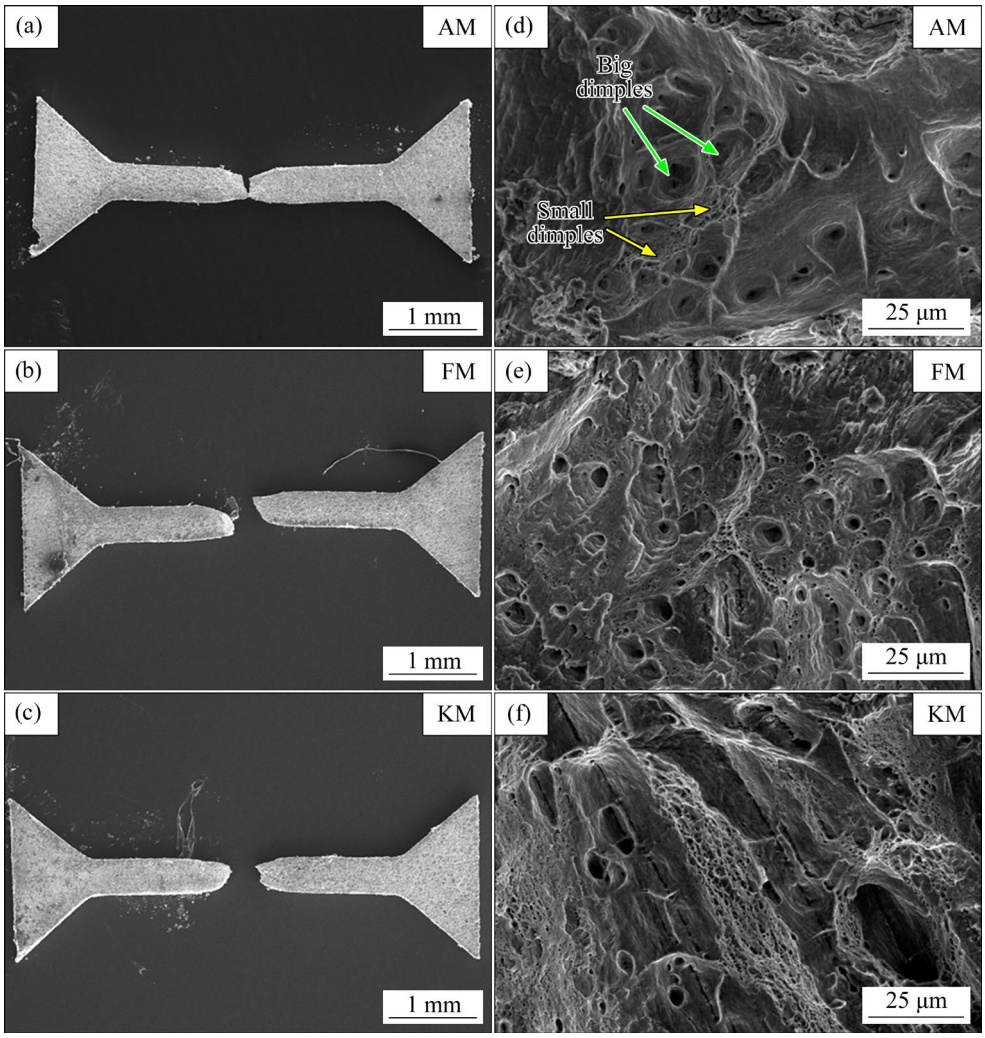

Fig. 13 Broken pieces (a−c) and fracture surfaces (d−f) of AM (a, d), FM (b, e), and KM (c, f) samples

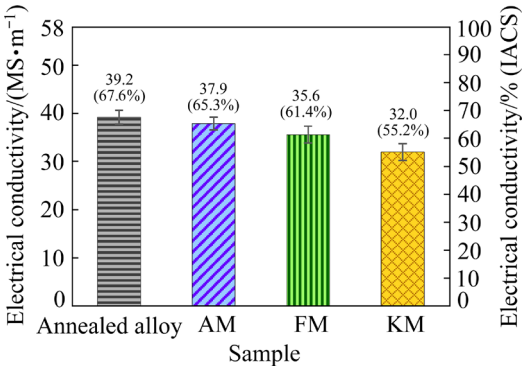

Fig. 14 Measured electrical conductivity values

was (39.2±2.5) MS/m (67.6% (IACS)), which is 32.4% lower than the conductivity of pure Cu (58 MS/m, 100% (IACS) [58]). This reduction demonstrates the significant detrimental impact of solid solution through Mg addition on electrical conductivity. This value was further reduced to (37.9±2.3) MS/m (65.3% (IACS)) after undergoing MaxStrain processing (AM sample). The FM and KM samples exhibited even lower electrical conductivities, with values of (35.6±3.0) MS/m (61.4% (IACS)) measured for the FM sample and (32.0±3.0) MS/m (55.2% (IACS)) measured for the KM sample. The 3%, 9%, and 18% decrease in electrical conductivity of the AM, FM, and KM samples compared to the annealed alloy, clearly demonstrates the negative effect of deformation strengthening on the electrical conductivity. In fact, the higher extent of DRXed grains in FM and KM samples provided a higher fraction of HAGBs in these samples (as shown in Fig. 10), which led to a lower electrical conductivity in these samples compared to the AM sample. Nevertheless, this negative effect was substantially lower than the detrimental impact of Mg-induced solid solution strengthening on the electrical conductivity. Remarkably, the KM sample, which experienced

the highest equivalent strain through deformation processes, exhibited the lowest electrical conductivity, while the AM sample, with the lowest equivalent strain, provided the highest electrical conductivity among all samples.

In conclusion, it is important to highlight that all MaxStrain-processed samples, with their electrical conductivities surpassing 50% (IACS) and favorable mechanical properties that they possessed, were eligible to be classified as HSHC Cu alloys based on the definition of HSHC Cu alloys by YANG et al [8]. However, it should also be noted that while MaxStrain processing serves as a valuable tool for analyzing the effects of various processing parameters on the microstructure, mechanical properties, and physical characteristics of metallic materials, it is not yet suitable for industrial applications. This limitation arises from factors such as its time-consuming nature, lack of continuity in production, and most importantly, the limited size of the product.

4 Conclusions

(1) The simulation of deformation processes demonstrated that the processing history had a critical influence in determining the equivalent strain attained in various regions of the deformed samples. Moreover, the results revealed that different distributions of equivalent strain obtained via forward extrusion and KoBo extrusion contributed to totally distinct equivalent strain distributions after MaxStrain processing.

(2) Following the MaxStrain processing, the initial coarse grain structure of the annealed alloy was fragmented to a heterogeneous grain microstructure consisting of coarse elongated as well as fine equiaxed grains as a consequence of the occurrence of partial DRX. The proportion of DRXed grains was observed higher in the FM and KM samples that, respectively, underwent forward extrusion and KoBo extrusion prior to MaxStrain processing. Moreover, EBSD results revealed that the fraction of HAGBs was higher in the FM and KM samples compared to the AM sample (solely subjected to MaxStrain processing), which was attributed to a higher extent of DRX.

(3) According to the tensile test results, the MaxStrain process increased the YS and UTS of the annealed alloy by 251% and 95%, respectively. In the meantime, FM and KM samples, respectively, demonstrated 288% and 360% increase in the YS, and 121% and 169% higher UTS compared to the initial annealed alloy. This was attributed to the lower grain size as a result of the higher extent of DRX in FM and KM samples, along with the higher degree of deformation strengthening.

(4) The initial annealed alloy had an electrical conductivity of (39.2±2.5) MS/m (67.6% (IACS)), and this value was reduced to (37.9±2.3) MS/m after MaxStrain processing (AM sample). In addition, the FM sample with a lower equivalent strain exhibited an electrical conductivity of (35.6±3.0) MS/m, whereas the KM sample with a higher equivalent strain showed an electrical conductivity of (32.0±3.0) MS/m. Considering the mechanical properties and the electrical conductivities obtained for MaxStrain-processed samples, all samples met the criteria to be classified as HSHC Cu alloys.

CRediT authorship contribution statement

Alireza KALHOR: Data curation, Formal analysis, Investigation, Methodology, Resources, Software, Validation, Visualization, Writing − Original draft, Writing − Review & editing; **Kinga RODAK:** Conceptualization, Formal analysis, Funding acquisition, Methodology, Project administration, Resources, Supervision, Validation, Visualization, Writing − Review & editing; **Marek TKOCZ:** Conceptualization, Investigation, Software; **Bartosz CHMIELA:** Data curation, Investigation; **Ivo SCHINDLER:** Data curation, Funding acquisition; **Łukasz POLOCZEK:** Data curation; **Krzysztof RADWAŃSKI:** Data curation, Investigation; **Hamed MIRZADEH:** Writing − Review & editing; **Marian KAMPIK:** Data curation.

Declaration of competing interest

The authors declare that they have no known competing financial interests or personal relationships that could have appeared to influence the work reported in this paper.

Declaration of Generative AI and AI-assisted Technologies in the Writing Process

During the preparation of this work, the authors used ChatGPT-3.5 in order to detect and correct any grammatical mistakes. After using this tool, the authors reviewed and edited the content as needed and take full responsibility for the content of the publication.

Acknowledgments

This work has been financially supported by Silesian University of Technology, Poland (No. 11/030/BK_23/1127), and VŠB – Technical University of Ostrava Czech Republic (No. CZ.02.1.01/0.0/0.0/17_049/0008399). The authors also gratefully acknowledge the valuable collaboration and technical support provided by the members of the Faculty of Materials Engineering at Silesian University of Technology, Poland, without which this investigation would not have been possible.

References

[1] LI Z M, LI X N, HU Y L, ZHENG Y H, YANG M, LI N J, BI L X, LIU R W, WANG Q, DONG C, JIANG Y X, ZHANG X W. Cuboidal γ' phase coherent precipitation-strengthened Cu−Ni−Al alloys with high softening temperature [J]. Acta Materialia, 2021, 203: 116458.

[2] XIA C, PANG Y, JIA Y, NI C, SHENG X, WANG S, JIANG X, ZHOU Z. Orientation relationships between precipitates and matrix and their crystallographic transformation in a Cu−Cr−Zr alloy [J]. Materials Science and Engineering A, 2022, 850: 143576.

[3] ZHOU J, HU B, LI B, DU Y, WANG J. Experimental investigation and thermodynamic modeling of Cu−Nb−Si system [J]. Transactions of Nonferrous Metals Society of China, 2023, 33: 824−838.

[4] YANG H, BU Y, WU J, FANG Y, LIU J, WANG H. Nanocompound-induced anti-softening mechanisms: Application to CuCr alloys [J]. Materials Science and Engineering A, 2022, 841: 143038.

[5] YOU C, ZENG L, GAO R, ZHANG X, WANG H. A dual heterogeneous laminated microstructure design for improving the mechanical properties and electrical conductivity of copper alloys [J]. Materials Characterization, 2022, 187: 111878.

[6] WU X, ZHANG J, WANG R, ZAFAR Z, LIU X, LIU Y, QIAN L, SUN L. Achieving high strength and high conductivity synergy through hierarchical precipitation stimulated structural heterogeneities in a Cu−Ag−Zr alloy [J]. Materials & Design, 2022, 219: 110777.

[7] CHU Z Q, WEI K X, WEI W, ALEXANDROV I V, AN X L, WANG D D, LIU X K. Simultaneously enhancing mechanical properties and electrical conductivity of Cu−0.5%Cr alloy as 5G connector material [J]. Journal of Alloys and Compounds, 2023, 948: 169750.

[8] YANG H, MA Z, LEI C, MENG L, FANG Y, LIU J, WANG H. High strength and high conductivity Cu alloys: A review [J]. Science China Technological Sciences, 2020, 63: 2505−2517.

[9] ABE Y, SEMBOSHI S, MASAHASHI N, LIM S H, CHOI E A, HAN S Z. Mechanical strength and electrical conductivity of Cu−In solid solution alloy wires [J]. Metallurgical and Materials Transactions A, 2023, 54: 928−938.

[10] KUMAR A, TANG Y, LI D Y, CHEN D L, LI W, LI Q Y. Influence of solution-hardening on the mechanical properties and wear resistance of copper alloys [J]. Wear, 2023, 523: 204869.

[11] DÖLLING J, HENLE R, PRAHL U, ZILLY A, NANDI G. Copper−based alloys with optimized hardness and high conductivity: Research on precipitation hardening of low-alloyed binary CuSc alloys [J]. Metals, 2022, 12: 902.

[12] BAN Y, ZHOU M, ZHANG Y, JIA Y, PANG Y, LI Y, TANG S, LI X, VOLINSKY A A, MARCHENKO E S. Abnormally high work hardening ability and excellent comprehensive properties of copper alloys due to multiple twins and precipitates [J]. Materials & Design, 2023, 228: 111819.

[13] HUA Y, LIU H, SONG K, WANG J, GUO Y, TIAN J, GUO H. Effect of cerium on microstructure, texture and properties of ultrahigh-purity copper [J]. Journal of Rare Earths, 2024, 42: 220−227.

[14] SONG J, LIU H, SONG K, HUA Y, PENG X, ZHOU Y, GUO X, CHENG C, ZHANG L, WANG G, TIAN A. The interactions of Ce−P on microstructure and mechanical properties in pure copper [J]. Materials Science and Technology, 2022, 38: 1482−1489.

[15] QIN Y, ZHUANG Y, LUO L, ZHANG Y, WU Y. Effect of alloying element Zr on microstructure and properties of Cu−Y_2O_3 composites [J]. Transactions of Nonferrous Metals Society of China, 2023, 33: 3418−3426.

[16] LI Y, XIAO Z, LI Z, ZHOU Z, YANG Z, LEI Q. Microstructure and properties of a novel Cu−Mg−Ca alloy with high strength and high electrical conductivity [J]. Journal of Alloys and Compounds, 2017, 723: 1162−1170.

[17] BACH J, STOIBER M, SCHINDLER L, HÖPPEL H W, GÖKEN M. Deformation mechanisms and strain rate sensitivity of bimodal and ultrafine-grained copper [J]. Acta Materialia, 2020, 186: 363−373.

[18] CABIBBO M. Nanoindentation twin-sensitive measurements and strengthening model of HPT OFHC 99.99% purity copper [J]. Materials Science and Engineering A, 2020, 785: 139348.

[19] LIU M, WANG B B, AN X H, XUE P, LIU F C, WU L H, NI D R, XIAO B L, MA Z Y. Friction stir additive manufacturing enabling scale-up of ultrafine-grained pure copper with superior mechanical properties [J]. Materials Science and Engineering A, 2022, 857: 144088.

[20] CAO Y, NI S, LIAO X, SONG M, ZHU Y. Structural evolutions of metallic materials processed by severe plastic deformation [J]. Materials Science and Engineering R: Reports, 2018, 133: 1−59.

[21] AN X H, WU S D, WANG Z G, ZHANG Z F. Significance of stacking fault energy in bulk nanostructured materials: Insights from Cu and its binary alloys as model systems [J]. Progress in Materials Science, 2019, 101: 1−45.

[22] ZHANG P, SHI J, YU Y, SUN J, LI T. Effect of cryorolling on microstructure and property of high strength and high conductivity Cu−0.5wt.%Cr alloy [J]. Transactions of Nonferrous Metals Society of China, 2020, 30: 2472−2479.

[23] HIGUERA-COBOS O F, CABRERA J M. Mechanical, microstructural and electrical evolution of commercially pure copper processed by equal channel angular extrusion [J].

Materials Science and Engineering A, 2013, 571: 103−114.

[24] LIU X, ZHUANG L, ZHAO Y. Microstructure and mechanical properties of ultrafine-grained copper by accumulative roll bonding and subsequent annealing [J]. Materials, 2020, 13: 5171.

[25] JAFARIAN H R, MAHDAVIAN M M, SHAMS S A A, EIVANI A R. Microstructure analysis and observation of peculiar mechanical properties of Al/Cu/Zn/Ni multi-layered composite produced by accumulative-roll-bonding (ARB) [J]. Materials Science and Engineering A, 2021, 805: 140556.

[26] SEIFOLLAHZADEH P, ALIZADEH M, ABBASI M R. Strength prediction of multi-layered copper-based composites fabricated by accumulative roll bonding [J]. Transactions of Nonferrous Metals Society of China, 2021, 31: 1729−1739.

[27] XU R, LIANG N, ZHUANG L, WEI D, ZHAO Y. Microstructure and mechanical behaviors of Al/Cu laminated composites fabricated by accumulative roll bonding and intermediate annealing [J]. Materials Science and Engineering A, 2022, 832: 142510.

[28] DONG H, CHEN Y, GUO Y, SHAN G, YANG G, HUANG L, LIU F, LI Q. A nanostructured Ag/Cu multilayered composite exhibiting high hardness and high electrical conductivity prepared by a novel multicomponent accumulative roll bonding [J]. Materials Characterization, 2023, 196: 112613.

[29] ABD EL AAL M I, KIM H S. Effect of the fabrication method on the wear properties of copper silicon carbide composites [J]. Tribology International, 2018, 128: 140−154.

[30] YAGHOUBI M A, ANJABIN N, KIM H S. Effect of Y_2O_3 nanoparticles on the evolution of the microstructure and mechanical properties of severely plastic deformed cu sheets during friction stir processing [J]. Metals and Materials International, 2023, 29: 2710−2725.

[31] ALVES FLAUSINO P C, SIQUEIRA CORRÊA E C, RODRIGUES PEREIRA P H, PAULINO AGUILAR M T, CETLIN P R. Thermal stability of copper processed by multidirectional forging: Effect of deformation amplitude and cumulative Strain [J]. Materials Science and Engineering A, 2022, 846: 143299.

[32] PAOLETTI C, SANTECCHIA E, CABIBBO M, REGEV M, SPIGARELLI S. Revisiting copper as a case study of creep in pure metals: Prediction of creep response in pure Cu in half-hard and friction-stir-processed states [J]. Materials Science and Engineering A, 2022, 832: 142426.

[33] HUANG J, ZHU Y T, ALEXANDER D J, LIAO X, LOWE T C, ASARO R J. Development of repetitive corrugation and straightening [J]. Materials Science and Engineering A, 2004, 371: 35−39.

[34] LEE H H, PARK H K, JUNG J, HWANG K J, KIM H S. Microstructural tailoring in reverse gradient-structured copper sheet using single-roll angular-rolling and subsequent annealing [J]. Materials Science and Engineering A, 2019, 764: 138258.

[35] BOHLULI H, LAKHI M, RAKHSHKHORSHID M. Experimental–numerical study of the effect of per pass applied strain on the electrical and mechanical properties of copper samples in twist extrusion process [J]. Metals and Materials International, 2023, 29: 2182−2196.

[36] PAN S, YU J, HAN J, ZHANG Y, PENG Q, YANG M, CHEN Y, HUANG X, SHI R, WANG C, LIU X. Customized development of promising Cu−Cr−Ni−Co−Si alloys enabled by integrated machine learning and characterization [J]. Acta Materialia, 2023, 243: 118484.

[37] TONG Y, LI S, ZHANG D, LI L, ZHENG Y. High strength and high electrical conductivity CuMg alloy prepared by cryorolling [J]. Transactions of Nonferrous Metals Society of China, 2019, 29: 595−600.

[38] MA M, LI Z, QIU W, XIAO Z, ZHAO Z, JIANG Y. Microstructure and properties of Cu−Mg−Ca alloy processed by equal channel angular pressing [J]. Journal of Alloys and Compounds, 2019, 788: 50−60.

[39] MA M, LI Z, QIU W, XIAO Z, ZHAO Z, JIANG Y, XIA Z, HUANG H. Development of homogeneity in a Cu−Mg−Ca alloy processed by equal channel angular pressing [J]. Journal of Alloys and Compounds, 2020, 820: 153112.

[40] RU Y, GAO Z, ZHANG L, TANG Z, ZUO T, XUE J, XIAO L, LI X. Microstructure and properties of high strength and high conductivity Cu−0.4Mg alloy processed by upward continuous casting and multi-pass drawing [J]. Journal of Materials Engineering and Performance, 2023, 33: 5041−5048.

[41] MEZBAHUL-ISLAM M, MOSTAFA A, MEDRAJ M. Essential magnesium alloys binary phase diagrams and their thermochemical data [J]. Journal of Materials, 2014, 2014: 704283.

[42] GORSSE S, OUVRARD B, GOUNÉ M, POULON-QUINTIN A. Microstructural design of new high conductivity–high strength Cu-based alloy [J]. Journal of Alloys and Compounds, 2015, 633: 42−47.

[43] BALAWENDER T, ZWOLAK M, BĄK Ł. Experimental analysis of mechanical characteristics of KOBO extrusion method [J]. Archives of Metallurgy and Materials, 2020, 65: 615−619.

[44] KORBEL A, BOCHNIAK W. Refinement and control of the metal structure elements by plastic deformation [J]. Scripta Materialia, 2004, 51: 755−759.

[45] OSTACHOWSKI P, BOCHNIAK W, ŁAGODA M, ZIÓŁKIEWICZ S. Strength properties and structure of CuCrZr alloy subjected to low-temperature KOBO extrusion and heat treatment [J]. The International Journal of Advanced Manufacturing Technology, 2019, 105: 5023−5044.

[46] BOCHNIAK W, OSTACHOWSKI P, KORBEL A, ŁAGODA M. Potential of the KOBO extrusion process for nonferrous metals in the form of solids and chips [J]. The International Journal of Advanced Manufacturing Technology, 2023, 127: 733−750.

[47] OSTACHOWSKI P, PALIBOREK A, BOCHNIAK W, ŁAGODA M. Mechanical characteristics and structure of highly deformed zinc [J]. Journal of Materials Engineering and Performance, 2022, 31: 3638−3660.

[48] KOMAROV V, KHMELEVSKAYA I, KARELIN R, PROKOSHKIN S, ZARIPOVA M, ISAENKOVA M, KORPALA G, KAWALLA R. Effect of biaxial cyclic severe deformation on structure and properties of Ti−Ni alloys [J]. Journal of Alloys and Compounds, 2019, 797: 842−848.

[49] KOMAROV V, KARELIN R, KHMELEVSKAYA I,

CHERKASOV V, YUSUPOV V, KORPALA G, KAWALLA R, PRAHL U, PROKOSHKIN S. Evolution of structure and properties of nickel-enriched NiTi shape memory alloy subjected to Bi-axial deformation [J]. Materials, 2023, 16: 511.

[50] KOMAROV V, KHMELEVSKAYA I, KORPALA G, KAWALLA R, PROKOSHKIN S. Metal forming aspects of cyclic severe plastic deformation of Ti−Ni shape memory alloys using Maxstrain device [J]. Key Engineering Materials, 2017, 746: 214−218.

[51] PETRYK H, STUPKIEWICZ S, KUZIAK R. Grain refinement and strain hardening in IF steel during multi-axis compression: Experiment and modelling [J]. Journal of Materials Processing Technology, 2008, 204: 255−263.

[52] MANDAL P, MONDAL S C. Investigation of electro-thermal property for Cu-MWCNT composite coating on anodized 6061 aluminium alloy [J]. Applied Surface Science, 2018, 454: 138−147.

[53] MOU X, PENG K, ZENG J, SHAW L L, QIAN K W. The influence of the equivalent strain on the microstructure and hardness of H62 brass subjected to multi-cycle constrained groove pressing [J]. Journal of Materials Processing Technology, 2011, 211: 590−596.

[54] ZHU C, MA A, JIANG J, LI X, SONG D, YANG D, YUAN Y, CHEN J. Effect of ECAP combined cold working on mechanical properties and electrical conductivity of Conform-produced Cu−Mg alloys [J]. Journal of Alloys and Compounds, 2014, 582: 135−140.

[55] RODRÍGUEZ-CALVILLO P, FERRER N, CABRERA J M. Analysis of microstructure and strengthening in CuMg alloys deformed by equal channel angular pressing [J]. Journal of Alloys and Compounds, 2015, 626: 340−348.

[56] JIANG L, FU H, ZHANG H, XIE J. Physical mechanism interpretation of polycrystalline metals' yield strength via a data-driven method: A novel Hall−Petch relationship [J]. Acta Materialia, 2022, 231: 117868.

[57] GUO T, QIAN D, HUANG D, LI K, GAO Y, DING Y. Deformation microstructure and properties control of Cu−0.6Cr alloy in cryo-equal channel angular pressing [J]. Journal of Central South University, 2023, 30: 2094−2106.

[58] TANG X, CHEN X, SUN F, LIU P, ZHOU H, FU S. The current state of CuCrZr and CuCrNb alloys manufactured by additive manufacturing: A review [J]. Materials & Design, 2022, 224: 111419.

加工历史对 Cu−0.7Mg 合金显微组织、力学性能和电导率的影响

Alireza KALHOR[1], Kinga RODAK[1], Marek TKOCZ[1], Bartosz CHMIELA[1], Ivo SCHINDLER[2], Łukasz POLOCZEK[3], Krzysztof RADWAŃSKI[3], Hamed MIRZADEH[4], Marian KAMPIK[5]

1. Faculty of Materials Engineering, Silesian University of Technology, Krasińskiego 8, 40-019, Katowice, Poland;
2. VŠB−Technical University of Ostrava, Faculty of Materials Science and Technology, 17. listopadu 2172/15, 70800 Ostrava, Czech Republic;
3. Materials Research Group, Łukasiewicz Upper Silesian Institute of Technology, Karola Miarki 12-14, 44-100, Gliwice, Poland;
4. School of Metallurgy and Materials Engineering, College of Engineering, University of Tehran, Tehran, Iran;
5. Faculty of Electrical Engineering, Silesian University of Technology, 44-100, Gliwice, Poland

摘　要：研究了正向挤压、与可逆扭转结合的挤压(KoBo 挤压)和通过 Gleeble 形变热模拟器的 MaxStrain 模块进行的额外变形对 Cu−0.7Mg (质量分数，%)合金显微组织、力学性能和电导率的影响。模拟结果表明加工历史在决定等效应变分布方面的关键作用。在 400 ℃下进行正向挤压并随后进行 MaxStrain 加工的样品(FM 样品)，其晶粒尺寸比仅经过 MaxStrain 加工的样品(AM 样品)小 76%。同样，经过 KoBo 挤压和 MaxStrain 加工样品(KM 样品)的晶粒尺寸比 AM 样品小 66%。拉伸测试结果显示，与初始退火态合金相比，AM、FM 和 KM 样品的屈服强度分别提高了 251%、288%和 360%，抗拉强度分别提高了 95%、121%和 169%，这主要是由于晶粒细化和形变强化的作用。最后，电导率检测结果显示，AM、FM 和 KM 样品的电导率分别为 37.9、35.6 和 32.0 MS/m。结合其力学性能考虑，这些样品符合高强高导铜合金的分类标准。

关键词：KoBo 挤压；MaxStrain 加工；等效应变计算；晶粒细化；拉伸性能；电导率

(Edited by Bing YANG)